Investigation of Porous Alumina as a Self-Assembled Diffractive Element to Facilitate Light Trapping in Thin Film Silicon Solar Cells

by

Naomi Coronel

Submitted to the Department of Materials
Science and Engineering in Partial
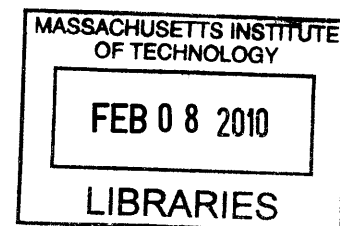Fulfillment of the Requirements for the
Degree of

Bachelor of Science

at the

Massachusetts Institute of Technology

June 2009

© 2009 Naomi Coronel

The author hereby grants to MIT permission to reproduce and to
distribute publicly paper and electronic copies of this thesis document in whole or in part
in any medium now known or hereafter created.

Signature of Author...
Department of Materials Science and Engineering
May 22, 2009

Certified by ....
Lionel C. Kimerling
Thomas Lord Professor of Materials Science and Engineering
Thesis Supervisor

Accepted by ....
Lionel C. Kimerling
Thomas Lord Professor of Materials Science and Engineering
Chairman, Undergraduate Committee

Abstract

Thin film solar cells are currently being investigated as an affordable alternative energy source because of the reduced material cost. However, these devices suffer from low efficiencies, compared to silicon wafer solar cells, due to the poor absorption of longer wavelengths of light in the very thin active layer. One method of improving the efficiency of thin film solar cells is to use light trapping to increase the path length of long wavelength light to increase the probability of absorption. Previous work has yielded a new light trapping design, the textured photonic crystal, which incorporates a backside distributed Bragg reflector with a diffraction grating for large-angle diffraction. This study develops a simple and cost-effective fabrication method of using porous alumina as a self-assembled textured photonic crystal. Porous alumina is an attractive material because under certain anodization conditions, the pores form an ordered array. The ordered pore structure on the surface can serve as a diffraction grating, while alternating the pore size could vary the refractive index and form a distributed Bragg reflector. In this thesis, the arrangement of pores on the alumina surfaces is determined using a Fourier transform analysis. Results show that the average interpore distance of the samples depends linearly on the anodization voltage during pore initiation. These results will help to understand the pore initiation process and control that process to minimize fabrication steps.

Table of Contents

Introduction to Solar Cells

The application of the diffraction element studied in this thesis is for the improvement of photovoltaic efficiency. Solar cells are a great source of unlimited and clean energy. The recent need to replace fossil fuels with alternative energy sources has boosted research in the area of photovoltaics with the ultimate goal of making solar energy as efficient and inexpensive as current fossil fuel energy.

Photovoltaic Effect

Solar cells rely on the photovoltaic effect, which is the transfer of energy from photons into electricity through electron excitation. Semiconductors have an energy barrier that valence electrons must overcome to be free for conduction. This barrier is the electronic band gap (E_g), and is equal to the difference between the highest valence band energy and the lowest conduction band energy. If an incoming photon has an energy that is larger than the bang gap energy, then a valence electron can absorb that energy and be excited into the conduction band. This is called carrier generation and the result is an electron-hole pair. An electron in the conduction band is able to move throughout a material and carry with it its negative charge; the same is true for holes in the valence band carrying positive charge. This flow of charge is the definition of an electric current.
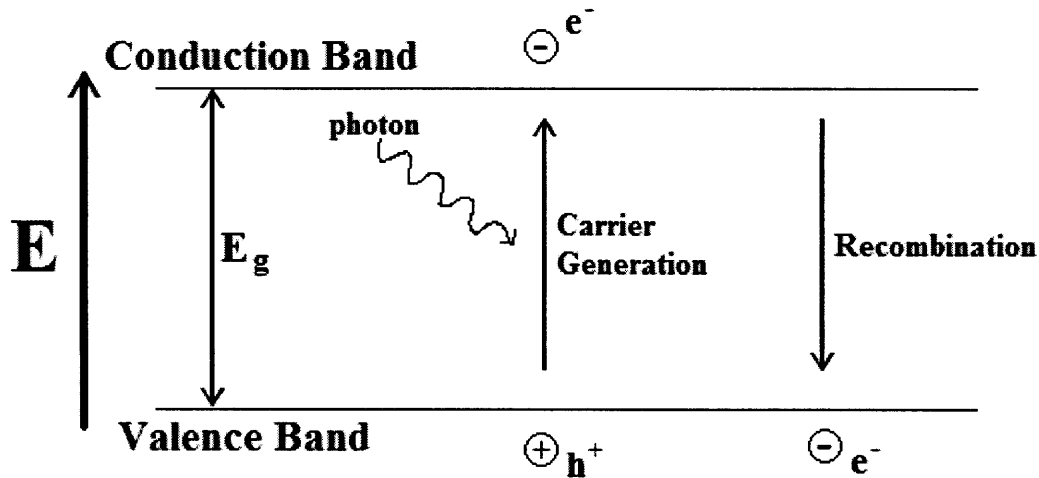
Figure 1. Semiconductor band structure describing the processes of carrier generation and recombination.

When an electron and a hole find themselves in the vicinity of each other, there is a possibility that they will recombine and release the energy gained from the photon. Therefore, once an electron-hole pair is created it is most efficient to separate the charges from each other as quickly as possible. This charge carrier collection is usually done with a p-n junction. Doping of semiconductors is the addition of impurity atoms to either increase the electron concentration (n-type doping) or increase the hole concentration (p-type doping) of a material. At the interface between an n-type region and a p-type region, electrons and holes diffuse down their respective concentration gradients so that electrons move into the p-type side and holes move into the n-type side. During this process, the electrons and holes leave positive and negative ions behind because the semiconductor atoms are not mobile. These ions generate an electric field with a potential gradient that counteracts the force of the concentration gradient. At some point, the two forces will balance each other out and there will be a small electric field, known as the built-in electric field, left at the p-n junction.
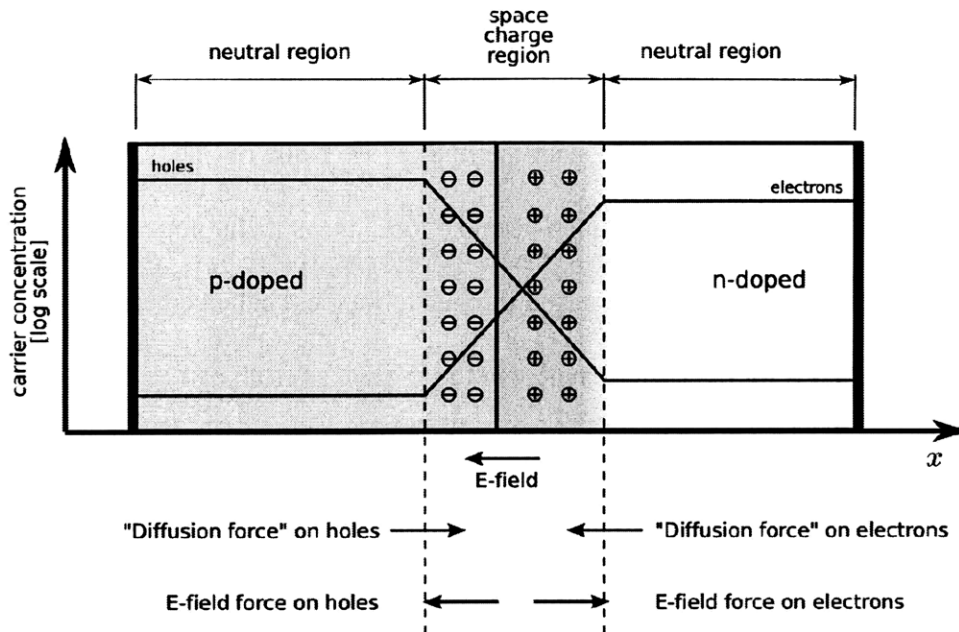
Figure 2. Forces in balance at a p-n junction interface. The diffusion force is due to a concentration gradient, and the E-field force is caused by immobile ions at the interface. [1]

When the junction is put under a reverse voltage bias, where the positive terminal is connected to the n-doped side, the electric field from the external voltage builds upon the built-in electric field. This results in an increase of the electric field force felt by the electrons and holes in the charged regions of the junction and an upset of the equilibrium state. When an electron-hole pair is formed near the p-n junction, the carriers will respond to the large electric field force and will quickly be swept in opposite directions. This electric field injects electrons into the n-doped region and holes into the p-doped region where they can continue in the circuit to power some load. By this method, energy from incoming light can be more efficiently converted into electrical current.

Current Solar Cell Technology

The most common solar cells now on the market are made of thick crystalline silicon wafers. They are relatively easy to produce because fabrication technology has already been put in place by the microelectronics industry, and they have the best balance between efficiency and cost. However, there is a lot of wasted energy in these devices from carrier recombination, and the cost of single-crystal silicon is very high (40-50% of the device cost) due to the difficulty in purifying and growing the material [2].

The other type of solar cell that is currently in production is a thin film solar cell. The semiconductor layer, which can be amorphous silicon, cadmium telluride, or copper indium (gallium) diselenide, is deposited on a glass substrate and is usually only a few microns thick. There are many advantages to using thin film devices over bulk devices. Thin film devices use very little material, so the material cost of the device is reduced. They can also be fabricated monolithically, which lowers fabrication costs and improves the efficiency of the factory. In addition, the small lengths make thin film devices less sensitive to the quality of the material because the thickness is on the order of the minority carrier diffusion length. Nevertheless, these thin film devices are much less efficient than thick crystalline silicon cells because the smaller thickness leads to a shorter path length for the incoming light and the probability of absorption is decreased. Therefore, thin film solar cells only account for about 7% of the market share, and they are mostly used for very low power applications [2].

Many people are still working to develop new solar cell technologies. These efforts include research in tandem cells, solar concentrators, sun-tracking systems, dye-sensitized

electrochemical cells, and polymer/organic solar cells. However, these technologies are not yet efficient enough or cost-effective enough to be produced on a large scale.

Light Trapping for Increased Efficiency

Most of the new solar cell technologies being studied are in the early stages of development and will not be ready for production any time soon. An alternate solution to creating completely new technologies is to improve on the efficiency of solar cells that are already in production. Some ways to improve efficiency are to match the bang gap of the active material to take advantage of the solar spectrum (shown in Figure 3), to increase the mobility of charge carriers to avoid recombination, and to enhance the absorption of incoming light. One way to enhance absorption is by light trapping. There is a lot of wasted energy from incoming photons that cannot be absorbed by the active material. By trapping light in the active region, the path length of the light is increased and the probability of absorption is therefore also increased. This enhancement would be especially useful for thin film solar cells because the active region of the device is already very small and can only effectively absorb light if the absorption length is less than the thickness (below about 800 nm) [4]. Figure 3 shows that the solar spectrum has a large region above 800 nm and the efficiency of thin film solar cells could be greatly improved by being able to absorb these wavelengths.
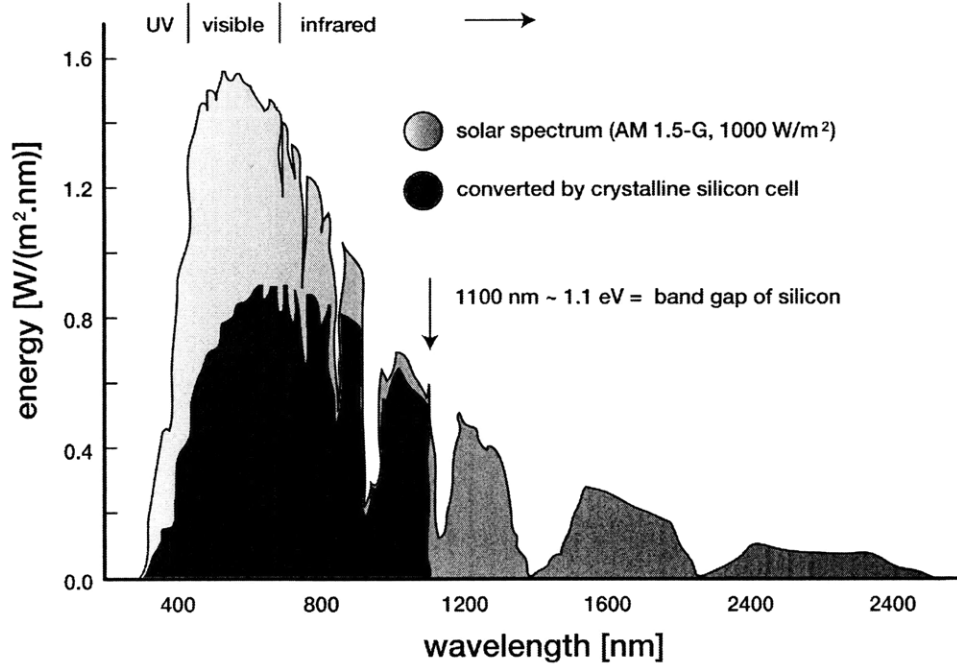
Figure 3. Solar spectrum. Indicates wavelengths absorbed by crystalline silicon [3].

Project Background

This thesis project follows from the work of Lirong Zeng in her Ph.D. thesis titled "High Efficiency Thin Film Silicon Solar Cells with Novel Light Trapping: Principle, Design and Processing" [4].

Textured Photonic Crystal

In her thesis, Lirong Zeng developed a new light trapping scheme for silicon photovoltaics. This novel design, which she called a textured photonic crystal, combines two forms of light trapping to improve device efficiency. The design incorporates a distributed Bragg reflector (DBR) as a reflective backside structure and a reflection grating for large-angle diffraction. It was shown that the total efficiency of a solar cell is greatly increased with integration of the textured photonic crystal than for integration with either a DBR or grating alone.
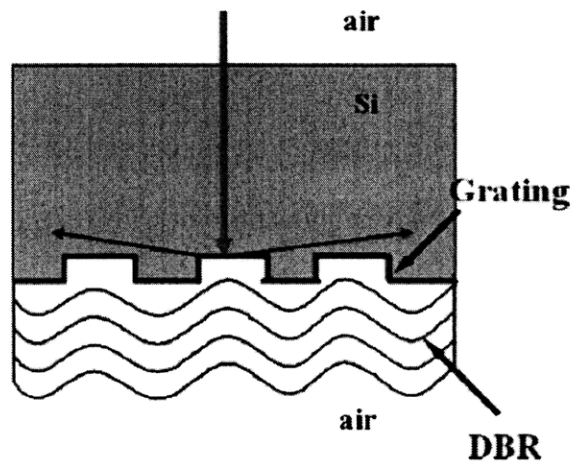

Figure 4. Schematic of the textured photonic crystal as designed by Lirong Zeng. Incoming light is diffracted at a large-angle into the plane of the device. [4]

The DBR is a one-dimensional photonic crystal made of alternating layers of two materials with contrasting refractive indices. At each interface within the stack, optical waves are partially reflected and the reflections can interfere constructively with each other to achieve near perfect reflection. The range of wavelengths that are not allowed to propagate through the layers defines the photonic band gap of the reflector. The properties of the photonic band gap can be tuned by using Eq. 1 through Eq. 3.

$$R = \left[\frac{n_2^{2N} - n_1^{2N}}{n_2^{2N} + n_1^{2N}} \right]^2 \qquad (1),$$

$$\Delta\lambda = \frac{\lambda_0}{\pi} \cdot \frac{(n_2 - n_1)(n_2 + n_1)}{n_1 n_2} \qquad (2), \text{ and}$$

$$t_{1,2} = \frac{\lambda_0}{4n_{1,2}} \qquad (3)$$

where R is the reflectivity of the DBR in air, N is the number of layer pairs in the stack, n_2 is the higher refractive index, n_1 is the lower refractive index, $\Delta\lambda$ is the width of the photonic band gap, λ_0 is the central wavelength of the band gap, and t is the thickness of a layer of one material. The DBR fabricated by Lirong was made by depositing layers of silicon and silicon dioxide or silicon and silicon nitride to achieve near 100% reflectivity. This process can be carried out with a dual-target sputtering chamber.

In thin film solar cells, since the path length depends on the number of reflections and the thickness of the active material, wavelengths of light with very large absorption lengths are still not able to be absorbed. The large-angle diffraction grating helps with this by directing the reflected light into the plane of the device instead of perpendicular to it. This effectively makes the path length on the order of the device size, which is much larger than the material thickness.

14

The direction that the light will travel in follows the equation for a diffraction grating shown in Eq. 4.

$$d\left(\sin \theta_m + \sin \theta_i\right) = m\lambda \qquad (4)$$

where d is the grating spacing, m is an integer representing the order of the diffracted light, θ_m is the angle of diffracted light of the mth order, θ_i is the angle of incident light, and λ is the wavelength. Lirong was able to use interference lithography to fabricate a grating with a pitch on the order of hundreds of nanometers. However, this kind of high-resolution fabrication processes is expensive.

Project Purpose

The purpose of this thesis project is to make the textured photonic crystal an efficient and marketable improvement for current solar cell technologies by simplifying the fabrication process and making the structure as cost-effective as possible. Some ideas of how to fabricate the textured photonic crystal were to use self-assembly of block copolymers to make the DBR, or soft lithography to stamp the grating pattern. However, for this thesis I looked at porous alumina which can act as both the DBR and grating structures. In an ideal case, the pores that form during anodization of aluminum would arrange themselves in a hexagonal honeycomb pattern. This periodic structure can act as a two-dimensional grating for large-angle diffraction. Also by changing the processing conditions during anodization, the diameter of the pores can be varied so that layers form with different refractive indices [5]. These layers can form a DBR structure. Figure 5 shows the ideal structure of a porous alumina textured photonic crystal. The added

benefit of using porous alumina is that under the right conditions the ordered pore arrangement would essentially be self-assembled.
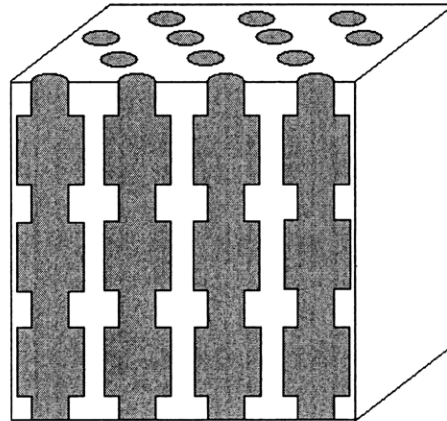

Figure 5. Ideal structure desired for a textured photonic crystal made from porous alumina. Pore size varies along the film thickness and the surface is periodic.

This thesis will focus on the feasibility of using the porous alumina films as a diffraction grating for large-angle reflection. The goal is to be able to fabricate the entire textured photonic crystal in as few steps as possible, which means anodization would be reduced to one step.
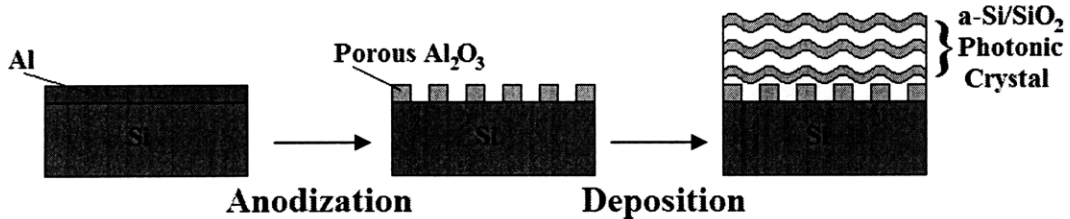

Figure 6. Fabrication of a textured photonic crystal using porous alumina as a diffraction grating.

Anodization

Aluminum can be oxidized into alumina (Al_2O_3) by using an anodization process. The aluminum film becomes the anode of the system and is put in an electrolyte solution containing a cathode as shown in Figure 7. For this project, phosphoric acid was used as the electrolyte, which becomes hydronium (H_3O^+) and phosphate ($H_xPO_4^{(3-x)-}$) when in an aqueous solution. On the aluminum film, there is already a thin native oxide layer from oxidation in air, which is only a few nanometers thick [6]. When a constant voltage is applied to the system, electrons are immediately stripped away from the aluminum atoms at the anode leaving Al^{3+} ions at the interface between the metal and the native oxide. At the cathode, electrons are injected into the electrolyte solution by reacting with H_3O^+ ions to form water and hydrogen gas. The applied voltage also causes an electric field to form from the aluminum to the electrolyte across the insulating native oxide layer. This electric field drives the flow of ion currents through the oxide, with Al^{3+} flowing towards the electrolyte and O^{2-} flowing towards the aluminum metal. At the interface between the oxide and electrolyte, Al^{3+} flows into the electrolyte solution and acts to balance out the negative charge left behind by the reacted H_3O^+ ions at the cathode. O^{2-} ions are also formed at this interface by a reaction between water and the phosphate ions in solution. On the metal side of the oxide layer, O^{2-} ions from the electrolyte solution react with the Al^{3+} ions to form more Al_2O_3, thereby increasing the oxide thickness in the direction of the aluminum metal.
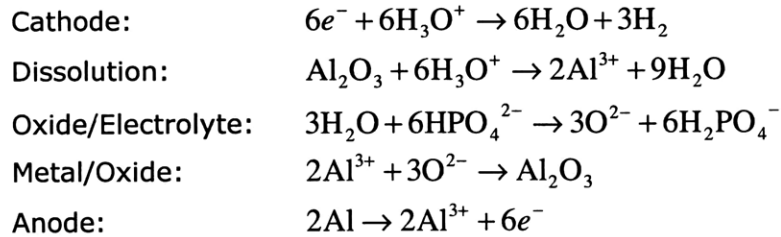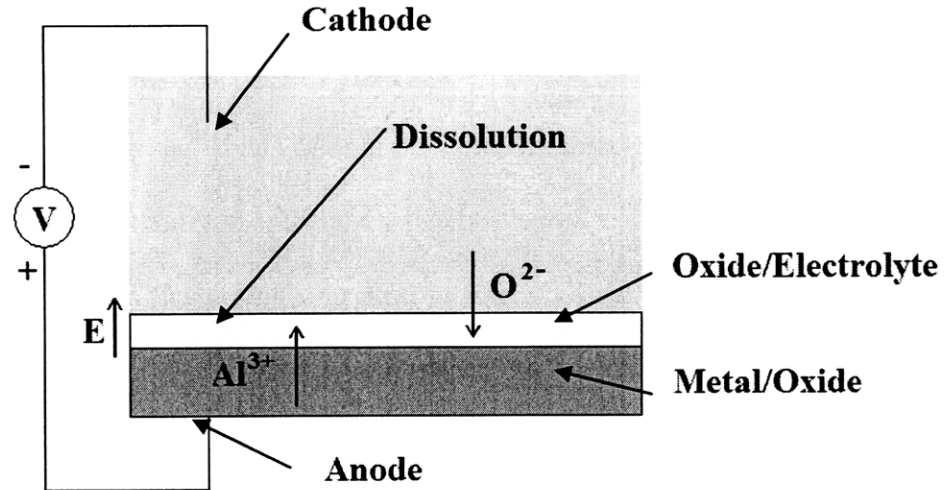
Cathode: $6e^- + 6H_3O^+ \rightarrow 6H_2O + 3H_2$

Dissolution: $Al_2O_3 + 6H_3O^+ \rightarrow 2Al^{3+} + 9H_2O$

Oxide/Electrolyte: $3H_2O + 6HPO_4^{2-} \rightarrow 3O^{2-} + 6H_2PO_4^-$

Metal/Oxide: $2Al^{3+} + 3O^{2-} \rightarrow Al_2O_3$

Anode: $2Al \rightarrow 2Al^{3+} + 6e^-$

Figure 7. Aluminum anodization in phosphoric acid electrolyte at constant voltage. Al^{3+} and O^{2-} ions travel through the Al_2O_3 barrier, driven by the electric field created by the applied voltage. Reaction equations are also shown to describe the process of anodization chemically.

In non-acid electrolyte solutions, the oxide grows in thickness until the electric field becomes too weak to drive any further ion currents and additional oxide cannot be created. By using an acid electrolyte (phosphoric acid), the oxide can also be dissolved at a rate that is comparable to the rate of oxide formation because of an increase in H_3O^+ concentration [6]. This leads to the formation of pores in the oxide film that allow the electric field to stay fairly constant and therefore allow the oxide to grow indefinitely. On the surface of the forming oxide, random perturbations from film deposition or solvent action create roughness such that the electric field is uneven across the entire film. Where there is a depression in the surface, the oxide thickness is smallest and the electric field will be higher than the surrounding area. Oxide will preferentially grow in these areas with a higher electric field because the ion currents are also higher. The

electric field also polarizes the ionic bonds between Al^{3+} and O^{2-}, which weakens the bond strength and makes it easier for H_3O^+ to dissolve the alumina, a process known as field-assisted dissolution [8]. For long anodization times, a steady-state condition is reached wherein the rate of oxide growth is equal to the rate of dissolution and the thickness of the oxide at the base of the pores is held constant.

After all of the aluminum has been oxidized, the structure of the porous alumina film will be made up of pores that penetrate the entire film thickness. A hexagonal honeycomb pattern is the ideal distribution of the pores, but this requires long anodization times and the correct process conditions. The arrangement of the pores becomes more periodic at the end of anodization than at the beginning because of the steady-state oxide growth condition that develops over time. Therefore, the surface of the oxide is likely to show a more random distribution of pores compared to the oxide at the interface with the substrate [7]. Also at the interface between the substrate and the porous alumina film, there will remain a thin, non-porous layer of oxide that is left over from the dielectric barrier during anodization. This layer is shown in Figure 8 with the thickness labeled as $t_{barrier}$. Further immersion in a phosphoric acid (or other solvent) solution can remove the remaining barrier oxide, but will also result in a larger pore diameter. Figure 8 also shows the relationship between different parameters in the pore structure. The spacing between pores (D_{int}) is the sum of the pore diameter (D_p) and twice the wall thickness (T)

$$D_{int} = D_p + 2T \qquad (5),$$

and it can also be shown that the ratio of T to $t_{barrier}$ is a constant, indicating a linear relationship between the two values [8].
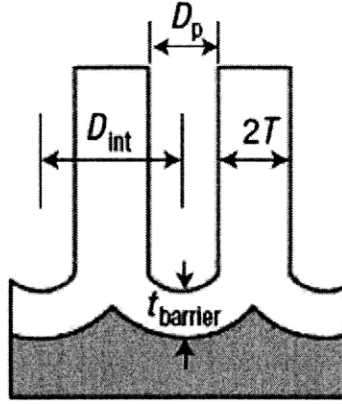
Figure 8. Pore structure after anodization in an acid electrolyte. D_p is the pore diameter, D_{int} is the interpore distance, T is the wall thickness, and $t_{barrier}$ is the oxide barrier thickness. [9]

The variables that can be controlled in this anodization process are voltage, temperature, and electrolyte concentration. The temperature and electrolyte concentration both determine the voltage at which the oxide film breaks down. For lower concentrations and temperatures, the solvent action is reduced and the oxide can withstand higher voltages. Varying the voltage changes D_{int}, the interpore distance. For larger voltages, the electric field can drive the same ion current through a larger barrier oxide thickness. Essentially, the oxide barrier acts like a capacitor and follows the equation for the electric field across a parallel-plate capacitor,

$$E = \frac{V}{d} \qquad (6)$$

where E is the electric field, V is the applied voltage, and d is the distance between the two plates ($t_{barrier}$). From Eq. 5, Eq. 6, and the known linear relationship between T and $t_{barrier}$, it can be concluded that D_{int} varies linearly with T, which varies linearly with $t_{barrier}$, and $t_{barrier}$ is linearly proportional to V, therefore the relationship between the anodization voltage and interpore distance should show a linear trend,

$$D_{int} \propto V \qquad (7).$$

The slope of the linear dependence for phosphoric acid anodization has been reported in several papers as 2.2 nmV^{-1} [8], 2.5 nmV^{-1} [9], 2.77 nmV^{-1} [8], and ~2 nmV^{-1} [10]. Figure 9 is a plot of interpore distance ("cell size") vs. voltage taken from one of these papers, which shows that the trend line does not pass through the origin. The authors of this paper speculate that there is some other factor affecting the interpore distance in addition to the voltage-dependence, but intercept seems to indicate that there is a critical cell size for pores to grow.
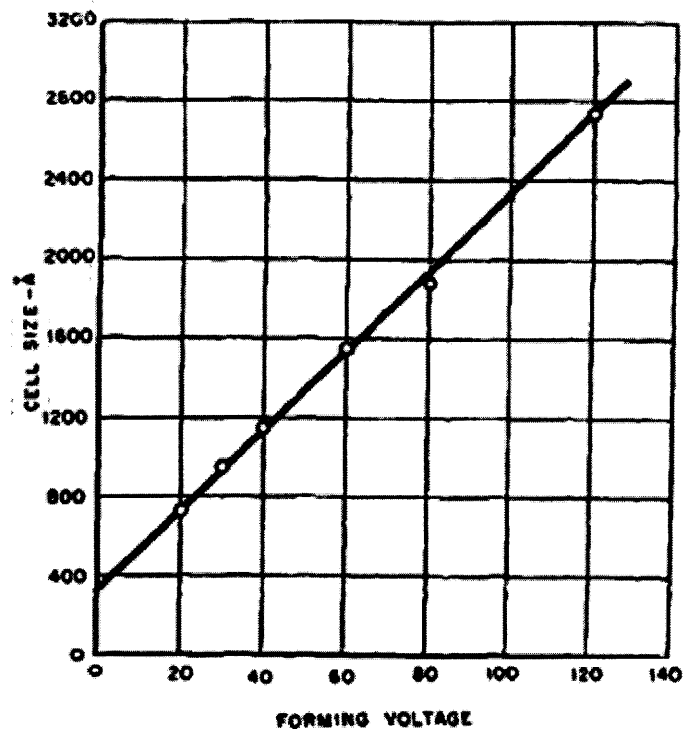

Figure 9. Interpore spacing ("cell size") vs. anodization voltage for anodization in 4wt% phosphoric acid solution. The slope of the linear fit is about 2 nmV^{-1} and the line does not pass through the origin, indicating a "nucleation and growth" type of process. [10]

Experimentation

Sample Preparation

Aluminum was deposited on silicon wafers by sputtering or e-beam deposition. The aluminum films were then anodized in a 4 percent by weight solution of phosphoric acid in water. Voltages ranged from 40 to 180 volts. For higher voltages, the anodizing cell was cooled to 5-10 degrees Celsius to prevent breakdown of the aluminum oxide. Films were left to anodize until all of the aluminum had become oxide, when a noticeable color change could be detected.

Diffraction Pattern Acquisition

A 488 nm argon laser was used to observe the diffraction pattern from the porous alumina films. The goal was to determine if the film would diffract at a large angle to help with light trapping. According to Eq. 4, the equation for grating diffraction, the 488 nm wavelength of the laser would not diffract if it were incident at an angle normal to the film surface. From the same equation, it is shown that an oblique incident angle would allow the observation of a diffraction pattern. This was tried on one of the porous alumina samples with the setup shown in Figure 10, and the result was that random scattering was observed in all directions instead of a well-defined diffraction pattern.
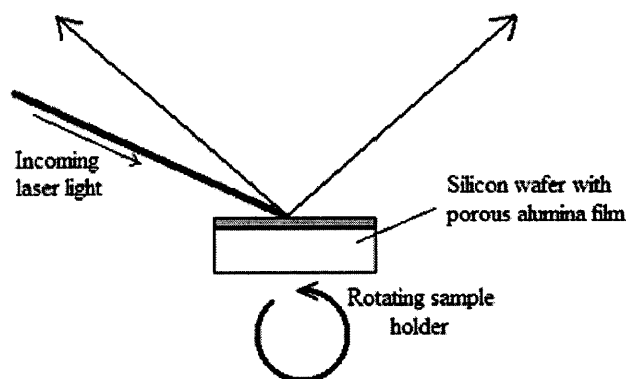
Figure 10. Laser setup for diffraction pattern acquisition. Laser light is 488 nm and sample holder can be rotated to get an oblique incident angle on the alumina film.

SEM Image Processing

To study the arrangement of the pore structure on the surface of the alumina films, scanning electron microscopy (SEM) was used to capture images of the film surfaces. Using an image editing software program, the images were converted to black and white to get the maximum contrast between the oxide surface and the pores. I then wrote a MATLAB program to analyze the black and white images using a discrete Fourier transform. The code for the MATLAB program is available in the Appendix. The two-dimensional discrete Fourier transform of an image translates the spatial domain into a frequency domain, where a repeating spatial pattern is shown as a point on the Fourier transform image. These points have values, representing the contrast within the spatial pattern, that determine the brightness of the point's pixel in the Fourier transform. An example of a transformation is shown in Figure 11. For perfectly periodic images, the Fourier transform consists of delta functions, where the spacing between objects in the real image is the reciprocal of the frequency of the delta function. If the

image is random, however, the transform will be comprised of a diffuse ring similar to rings in the diffraction patterns of amorphous or glassy materials. For these random Fourier transforms, the average spacing between objects in the original image is the reciprocal of the frequency represented by the radius of the diffuse ring. Also, how spread out the points are from the average radius can give an indication of the variation from the average spacing.
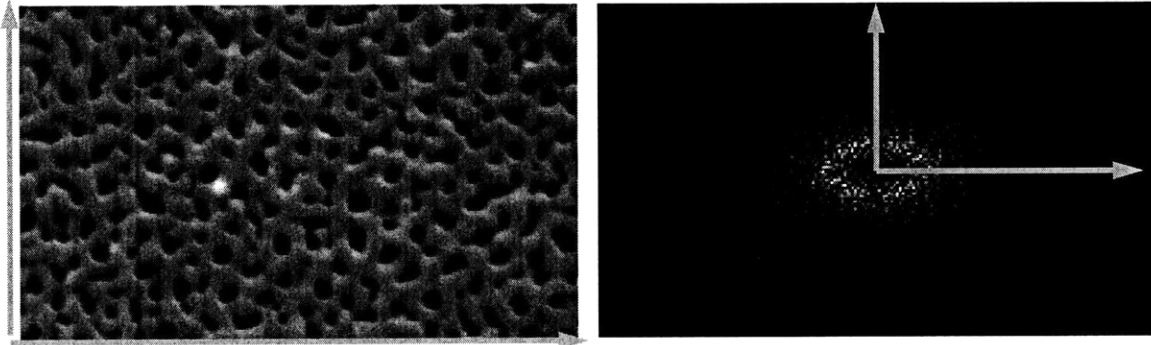

Figure 11. Discrete Fourier transform changes spatial domain to frequency domain. Points in the Fourier transform (right) are spatial frequencies present in the original image (left). For random pore arrangements, the Fourier transform is a diffuse ring where the ring radius should correspond to the average interpore spacing.

After calculating the discrete Fourier transform of one of the black and white images, the MATLAB program then normalizes the pixel values in the transform by the maximum value so that every point in the frequency space has an integer value between 0 and 255, which is the range of brightness for a digital image. Using the Pythagorean Theorem, the distance of each pixel from the center of the Fourier transform is calculated to get the frequency irrespective of direction. The pixel brightness and directionless frequency are only stored for pixels with a value above a threshold of ten. Because this data will be fit with a Gaussian peak and is very jagged and noisy as-is, the MATLAB program then filters through the data and only keeps the points with the highest pixel brightness values within each frequency increment of 0.001 px^{-1}. The final set of data points is output by MATLAB as an array of frequency and brightness values, which could then be plotted with the frequencies on the x-axis and the pixel brightness

values on the y-axis. Using a curve fitting program, the Gaussian distribution of the points was found, taking note of the frequency at the center of the peak and the full width at half maximum (FWHM). A plot of data points with the Gaussian peak fit is shown in Figure 12. From the frequency at the center of the peak, the average interpore distance was calculated by taking the reciprocal of the frequency value and converting the units to nanometers, using the scale bars on the original SEM images. The FWHM was then used as an indication of the variation in pore spacing from the average interpore distance.
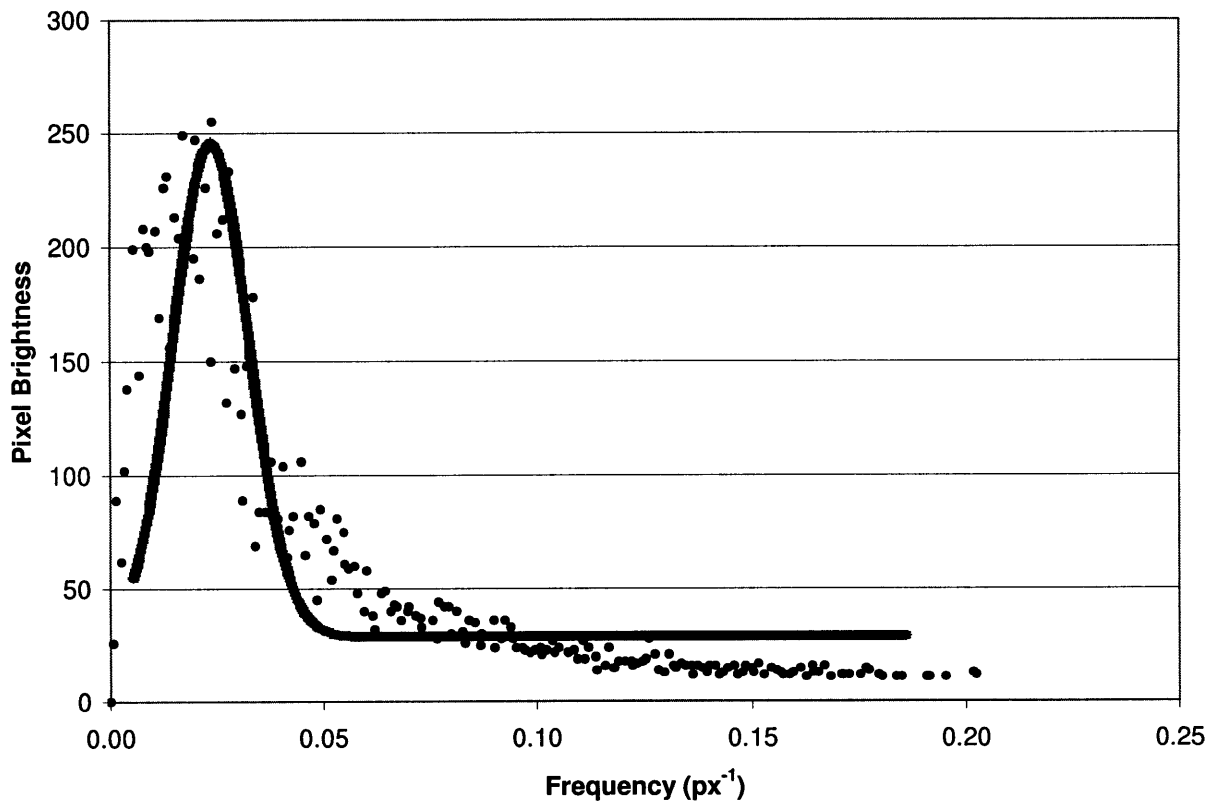
Figure 12. Pixel brightness vs. frequency for a random pore arrangement. The Gaussian peak fit is also shown, where the frequency at the peak center is the average interpore spacing and the full width at half maximum indicates the variation in pore distance from the average.

Results and Discussion

From the laser diffraction test, it was discovered that the porous alumina films act as random scatterers rather than ordered diffractive structures. This shows that the pores on the surface of the film are not periodic and instead are oriented in a random pattern. One of the problems with the laser diffraction test is that the surface of the porous alumina is very rough, in addition to being non-periodic, because of the time spent during anodization in harsh conditions resulting from the solvent action of the electrolyte solution and the heat generated from the anodization process. It is unclear whether the alumina films scatter randomly because of the random distribution of pores or because of the roughness on the surfaces. In the future, it would be valuable to try polishing the alumina surfaces before the laser diffraction test to rule out surface roughness as the cause of random scattering. Also, the surface of the alumina film in contact with the silicon substrate should be much more ordered than the top surface, and this is also the surface that will be used for diffraction in the actual photovoltaic device. To determine how the photovoltaic devices will diffract, there will need to be a comparison made of the behavior of the substrate interface with that of the top surface. By understanding the relationship between the surfaces of the alumina films, it may be possible to predict the diffractive behavior of the photovoltaic devices only by analyzing the accessible surface.

Figure 13 shows the calculated average interpore distance in real-space as a function of anodization voltage. From Eq. 7 and the literature review, there should be a linear dependence of the interpore distance on voltage with a slope of between 2 and 3 nmV^{-1}. A linear fit of the interpore distance data in Figure 13 gives a slope of 1.26 nmV^{-1}, which is much lower than the literature values. The difference is likely due to the fact that the oxide formation is not at a

steady-state condition during pore initiation on the surface, therefore the rate constant will be different from the steady-state value. Since the barrier oxide is not as thick as the steady-state thickness during the initial stages of oxide growth, the interpore spacing will be proportionally smaller, resulting in a smaller change in D_{int} per unit of voltage. The data in Figure 13 also agrees with the plot from the literature shown in Figure 9 in that the trend line does not pass through the origin. Figure 13 shows an intercept of 134.71 nm at 0V, while Figure 9 shows an intercept at about 30nm. This data suggests that there is a minimum spacing for pores to form.
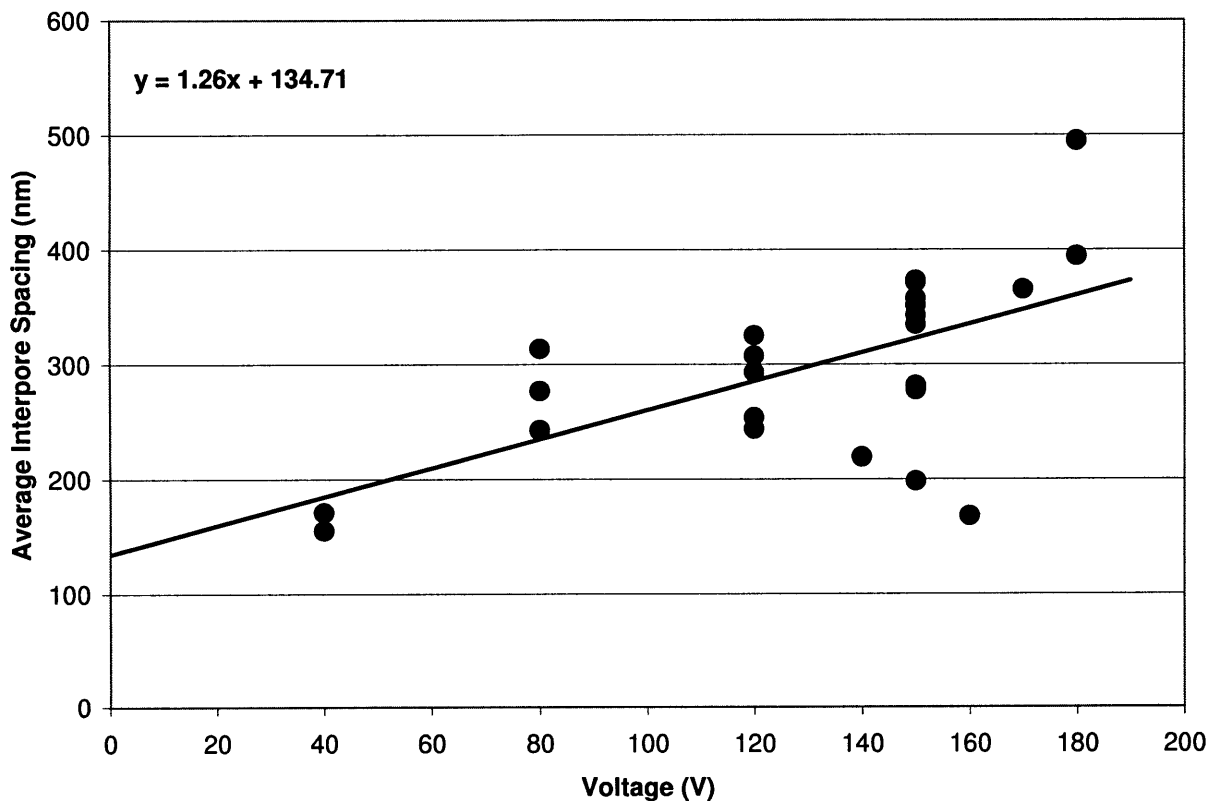

Figure 13. Dependence of interpore spacing on anodization voltage. Each point is the smallest value for one sample image, which should correspond to the nearest neighbor pore spacing, and gives a linear dependence of 1.26 nmV^{-1} and a y-intercept of 134.71 nm.

In analyzing the variation in pore spacing from the average interpore distance, I plotted the FWHM values, converted to nanometers, against the anodization voltage. This plot is shown

in Figure 14a, and follows a linear trend with variation decreasing as voltage is increased.

However, the slope of the line has the units of $nm^{-1}V^{-1}$, which is not a direct measure of the real-

space variation in interpore distance. To correct for this, I also calculated the variation is real-

space distance with the equation,

$$d_1 - d_2 = \frac{1}{f_c - \dfrac{FWHM}{2}} - \frac{1}{f_c + \dfrac{FWHM}{2}} = \frac{f_2 - f_1}{f_1 f_2} \qquad (8)$$

where d_1 is the maximum pore distance, d_2 is the minimum pore distance, f_c is the frequency at

the center of the peak, f_2 is the maximum frequency, and f_1 in the minimum frequency. As Eq. 8

shows, the range of interpore distances is not simply equal to the reciprocal of the range of

frequencies, and it depends on the actual values of the frequencies as well. The variation in real-

space interpore distance is shown in Figure 14b, and does not seem to follow a linear trend. It

seems that on the surface of the films the voltage does not have a great effect on the variation

because pore initiation occurs from random perturbations in oxide thickness.
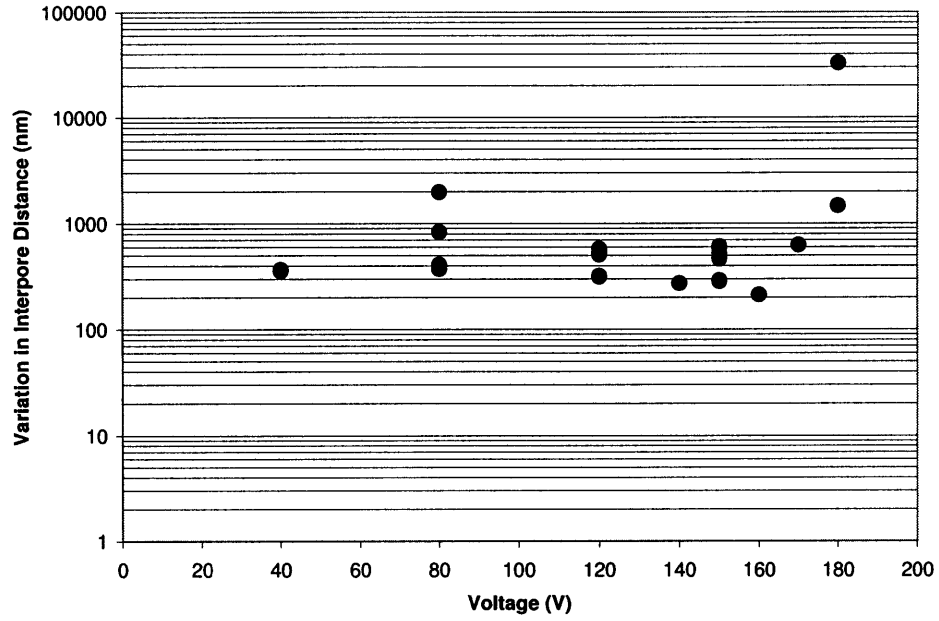
a)
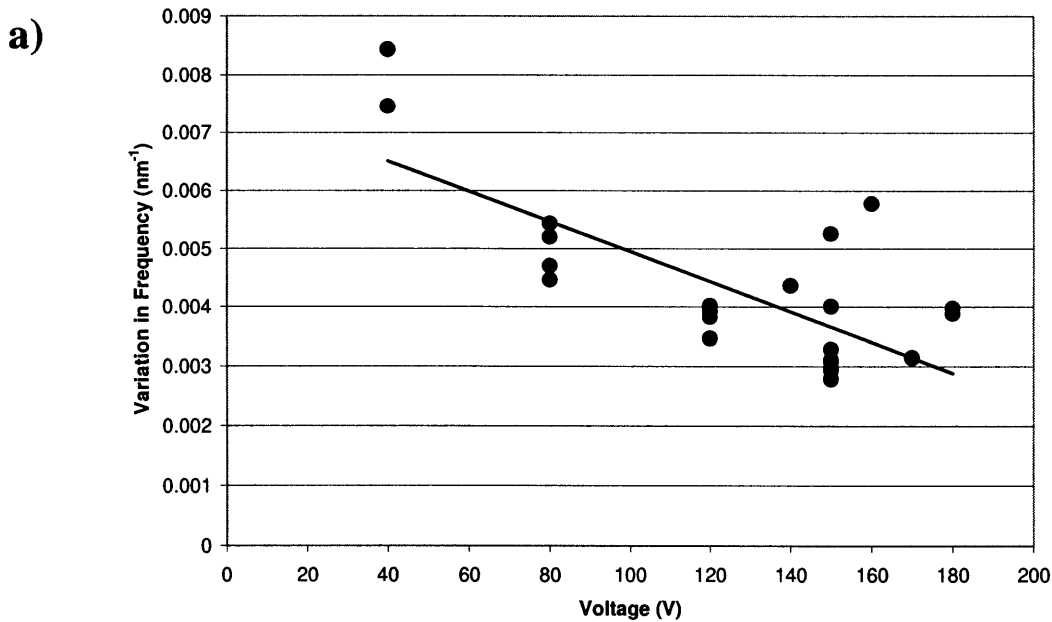
Figure 14. Variation in frequency and real-space distance as a function of anodization voltage. a) Plot shows frequency variation which appears to be linear. b) Plot shows real-space variation, which is not linear and is plotted on a semi-log scale because the range of values is very large.

Future Work

There is still a lot of work that can be done in determining the feasibility of using self-assembled porous alumina as a textured photonic crystal. In the near future, the focus will be on developing the fabrication process consisting of anodization of a thin film of porous alumina, to serve as a diffraction element, and deposition of a Si/SiO_2 photonic crystal. The challenge for this process is to create an ordered pore structure during the initial stages of anodization and pore formation. Eventually, the photonic crystal deposition step may not be required if the porous alumina can also act as DBR, reducing the textured photonic crystal fabrication to a one-step process. Therefore, an investigation of the porous alumina DBR fabrication process can also be a future project.

Thin Film Porous Alumina as a Diffraction Element

To fabricate a thin film of porous alumina, the initial stages of pore formation need to be understood because for anodization of a thin film, the entire process is essentially in the initial stage. One way to better understand anodization is to grind and polish thick anodized films to various depths and analyze the pore structure on these different levels of the porous alumina. From this analysis, we can determine how the pore structure changes over time. With an understanding of the pore initiation and growth processes, it may be possible to control the anodization conditions so that an ordered arrangement of pores is consistent throughout the thickness of the film.

A possible technique for controlling the pore formation process is to manually initiate the pores. Manual initiation can be one of two methods: double anodization or stamping. Double anodization takes advantage of the fact that the pore structure becomes more ordered as the anodization time is increased. For this method, anodization is first carried out in the same manner as this thesis, but is stopped as soon as the pores arrange themselves as desired. At this point, the oxide can be removed with a concentrated solution of phosphoric acid and the surface of the metal will have grooves left over from the bases of the pores. Upon a second anodization, these grooves will become the sites of new pores and the entire process will follow the pattern set by the first anodization. For the stamping method, the surface of the deposited aluminum is stamped with the desired pattern of pores, and as long as the anodization conditions can support the pattern, the pores will form in the stamped grooves. Unfortunately, both of these methods add an extra step to the fabrication process, so it would still be more cost-effective if an ordered thin film of porous alumina could be formed directly by anodization.

Porous Alumina as a Photonic Crystal

By alternating the voltage during the anodization process, the refractive index of the alumina can be changed [5]. A larger voltage will result in a larger pore spacing, which means that the ratio of air to alumina will be low. In this layer the refractive index will be closer to that of solid alumina. Conversely, a smaller voltage will decrease the pore spacing and increase the number of pores. This results in a larger ratio of air to alumina and the refractive index will be closer to that of air. By alternating these conditions, the porous alumina film will contain alternating layers of materials with different refractive indices, and can act as a DBR. The

effectiveness of a porous alumina DBR would need to be characterized and appropriate

anodization conditions found.

References

[1]   "p-n junction." Available at: http://en.wikipedia.org/wiki/P-n_junction.

[2]   "Solar Cell Technologies." Available at: http://www.solarbuzz.com/Technologies.htm.

[3]   "Vic Physics Events." Available at: http://www.vicphysics.org/events/stav2005.html.

[4]   Lirong Zeng, " High Efficiency Thin Film Silicon Solar Cells with Novel Light Trapping:
        Principle, Design and Processing " (PhD thesis, Massachusetts Institute of
        Technology, 2008).

[5]   Wang, B., Fei, G. T., Wang, M., Kong, M. G., and Zhang, L. D. Preparation of photonic
        crystals made of air pores in anodic alumina. *Nanotechnology, 18 (2007).*

[6]   "Electrochemistry Encyclopedia: Anodizing." Available at:
        http://electrochem.cwru.edu/encycl/art-a02-anodizing.htm.

[7]   Masuda, H., Yada, K., and Osaka, A. Self-Ordering of Cell Configuration of Anodic
        Porous Alumina with Large-Size Pores in Phosphoric Acid Solution. *Jpn. J. Appl.
        Phys., 37 (1998) pp. L 1340–L 1342.*

[8]   O'Sullivan, J. P. and Wood, G. C. The morphology and mechanism of formation of
        porous anodic films on aluminum. *Proc. Roy. Soc. Lond. A., 317 (1970) pp. 511-
        543.*

[9]   Lee, W., Ji, R., Gosele, U., and Nielsch, K. Fast fabrication of long-range ordered porous
        alumina membranes by hard anodization. *Nature Materials, 5 (2006).*

[10]   Keller, F., Hunter, M. S., and Robinson, D. L. Structural Features of Oxide Coatings on
        Aluminum. *Journal of the Electrochemical Society, 100 No. 9 (1953).*

Appendix

MATLAB code:

```
%retrieve image data
imname = 'image filename';
im = imread(imname);


%get the 2D fourier transform of the image
F = abs(fftshift(fft2(im)));


%set center pixel to 0
ycent = floor(size(F,1)/2+1);
xcent = floor(size(F,2)/2+1);
F(ycent,xcent) = 0;


%normalize to maximum value in Fourier transform
m = max(F(:));
A = round(F.*(255/m));


%get minimum pitch in y & x
pminy = min(factor(size(A,1)));
pminx = min(factor(size(A,2)));


%remove directionality of frequency
numpx = sum(sum(A>10))/2;
B = zeros(numpx,3);   %create matrix of all values >10
n = 0;   %row in B
for j=3:ycent
    for i=3:size(A,2)-2
        if j==ycent && i==xcent
            break   %only look through top half of image
        end
        if A(j,i)>10
            n = n + 1;
            fx = abs(i-xcent)/(xcent * pminx);
            fy = abs(j-ycent)/(ycent * pminy);
            B(n,1) = sqrt((1/fx^2)+(1/fy^2));   %store frequency
            B(n,2) = A(j,i);   %store pixel brightness
        end
    end
end


%remove noise by only keeping high points within frequency increments
B = sortrows(B,1);   %sort B in ascending order
mB = max(B);
C = zeros(floor(mB(1)*1000)+1,2);   %create matrix of increments
inc = 0.001;   %increment size
n = 1;   %row in B
m = 1;   %row in C
while n <= size(B,1)
    while B(n,1) < inc
        if B(n,2) > C(m,2)
            C(m,1) = B(n,1);   %store frequency
```

```
            C(m,2) = B(n,2);   %store pixel brightness
        end
        n = n + 1;
        if n > size(B,1)
            break
        end
    end
    inc = inc + 0.001;
    m = m + 1;
end
```